Volume 16, Issue 1, 162505 (1-9)

International Journal of Industrial Chemistry (IJIC)

https://doi.org/10.57647/j.ijic.2025.1601.05

Synthesis and isotherm studies of nGO@nFe_3O_4 decorated with ZIF-8 for methylene blue removal

Kaveh Pezeshk[1], Maryam Khavarpour[1,*], Seyed Mohammad Vahdat[2], Seyed Meysam Baghbanian[2], Mehri Esfahanian[3]

[1]*Department of Chemical Engineering, Ayatollah Amoli Branch, Islamic Azad University, Amol, Iran.*
[2]*Department of Chemistry, Ayatollah Amoli Branch, Islamic Azad University, Amol, Iran.*
[3]*Department of Chemical Engineering, Qaemshahr Branch, Islamic Azad University, Amol, Iran.*

[*]**Corresponding author:** mkhavarpoor@yahoo.com

Original Research

Received:
16 February 2025
Revised:
24 May 2025
Accepted:
28 May 2025
Published online:
29 May 2025

Abstract:

As the use of dyes in various industries has increased, environmental pollution has also increased due to the discharge of their wastewater into the waters. Here, the nanographene oxide@nano Fe_3O_4 (nGO@nFe_3O_4) decorated with ZIF-8 was synthesized to remove methylene blue from aqueous solutions. Physicochemical, thermal, morphological, and magnetic properties of ZIF-8@nGO@nFe_3O_4 nanocomposite adsorbent were characterized by standard analyses. SEM analysis show a porous structure and superposition of the layered structure of nGO@nFe_3O_4 which ZIF-8 was dispersed uniformly on or between the layers. Fine synthesis of the adsorbent was also confirm by FTIR. Results demonstrate the suitable growth of ZIF-8 on the surface of nGO@nFe_3O_4. The adsorbent possessed the appropriate magnetic ability and easily separated by a magnet. In addition, isotherm models of Langmuir, Freundlich, Temkin, and Redlich-Peterson were studied. Results show that Langmuir isotherm is the better model for describing the adsorption process, so, the adsorbent possesses a homogeneous surface, and the adsorption process is monolayer.

Keywords: Methylene blue; ZIF-8; Nanographene oxide; Magnetic; Isotherm

1. Introduction

Dyes and pigments are widely applied in various industries such as pharmaceutics, food, printing, textiles, etc. However, the discharge of their effluents/wastewaters into receiving waters is known as the main source of environmental pollution [1, 2]. In this field, treatment processes like chemical, physical, or biological separations play a crucial role in removing dyes from such wastewater, nonetheless, some dyes are chemically resistant and in mentioned industries, cause disposal problems [3]. Using technologies of membranes, reverse osmosis, and ion exchange, although effective, also requires high energy for treatment [4, 5]. Based on the reports, given that most dyes usually possess good stability against light and oxidizing agents, the adsorption systems can be more suitable options to treat wastewater owing to flexibility system, low-cost processing, ease of process, and greater efficiency [6, 7]. Moreover, the adsorption processes can provide high-quality effluents by managing fairly large rates of flow. In this field, many adsorbents have been designed, each with specific characteristics and capable of removing dye, heavy metals, and pollutants with varying adsorption capacity. Activated carbon, graphene oxide, biomasses, clay minerals, simple and magnetic nanoparticles, metal-organic framework, metal oxides, etc. are examples of this type of adsorbents [2, 8–11]. However, in recent years, the use of some of these materials has developed due to their unique properties.

Graphene oxide (GO) is one of these adsorbents that possesses an extremely high surface area and provides a large capacity for adsorbing pollutants [12]. This material also has high chemical reactivity, so that the presence of oxygen-containing groups such as hydroxyl, epoxy, and carboxyl on its surface increases its interaction with pollutants [13]. Moreover, the characteristics of mechanical strength, flexibility, environmental compatibility, porous structure, and high stability under various environmental conditions have promoted the expanded use of GO in various adsorption systems [14]. In this field, Elgengehi et al. reported that graphene and GO can be used as a suitable adsorbent to re-

move heavy metals (cadmium and lead). However, oxygen functional groups on GO led to a better stabilization of the metal binding than graphene [13].

Iron oxide (Fe_3O_4) is another sample in this field that can provide suitable properties for adsorbents applied in the environment and biomedicine industries, due to chemical stability and biocompatibility [10]. Indeed, the Fe3O4 has magnetic properties, enabling easy separation of the adsorbent after the adsorption process using a magnetic field [15, 16]. This material also possesses a high surface activity that can effectively interact with and adsorb various pollutants [17, 18]. In this matter, Mittal et al. indicated that Fe3O4-reinforced gum ghatti nanocomposites with a maximum adsorption capacity of 654.87 ppm, can be suitable adsorbents for removing rhodamine B [18].

ZIF-8 as a type of metal-organic framework (MOF) also is one of the other adsorbents that due to its porous structure and high stability under various conditions, has a wide range of applications, especially for the adsorption of pollutants, heavy metals, and organic compounds [19]. This material can also be combined with or modified by other materials to enhance its adsorption efficiency [20]. According to Chang et al., ZIF-8-modified GO/sodium alginate spheres play an important role in uranium removal trapping in seawater by swelling [21]. However, based on the reports, the adsorption efficiency for nano-adsorbents is higher than other adsorbents. It can be due to higher surface area, faster adsorption rate, better dispersion, or stronger magnetic properties of nanocomposite adsorbents along with reducing risk of particle aggregation [22].

Given the importance of the subject and the widespread application of nanomaterials in the synthesis and design of new adsorbents, this research aims to develop a nanocomposite adsorbent containing three materials of nano Go (nGO), nano Fe_3O_4 (nFe_3O_4), and ZIF-8 to remove the dye. To this end, ZIF-8 was first synthesized and then combined with nGO-nFe_3O_4 to reach to ZIF-8@nGO@nFe_3O_4 nanocomposite adsorbent. Afterward, the physicochemical, thermal, morphological, and magnetic characteristics of the adsorbent along with 4 other samples (ZIF-8, nGO, nFe_3O_4, and nGO@nFe_3O_4) were assessed by analyses of X-ray diffraction (XRD), Fourier-transform infrared spectroscopy (FT-IR), energy dispersive X-ray (EDS), thermogravimetric (TG), field emission scanning electron micrograph (FE-SEM), and vibrating sample magnetometer (VSM) analyses. The studies of the adsorption isotherm was also carried out to determine the capacity of adsorption.

2. Materials and methods

2.1 Materials

Zinc nitrate [$Zn(NO_3)_2.6H_2O$, 99.99%], nano graphene oxide [nGO], iron oxide (III) [Fe_3O_4], 2-methylimidazole, methylene blue [C16H18N3SCl], glutaraldehyde, hydrochloric acid [HCl], sodium hydroxide [NaOH], and acetic acid [CH_3-COOH], were all purchased from Merck company (Germany).

2.2 Methods

2.2.1 Synthesis of ZIF-8

2.93 g of zinc nitrate and 6.49 g of 2-methylimidazole were separately dissolved in 200 mL of methanol as solvent, under a stirrer (25 °C, 20 min). In the following, zinc nitrate solution was gradually added to 2-methylimidazole solution and mixed for 3 hours [23]. Subsequently, ZIF-8, white precipitate, was separated by centrifugation (5000 rpm, 5 min), and then washed with methanol 3 times. Finally, ZIF-8 crystals were obtained after drying in an oven (40 °C) for 12 h.

2.2.2 Preparation of nGO@nFe_3O_4

0.5 g of both nanographene oxide [nGO] and nano iron oxide [nFe_3O_4] were separately added to 100 mL of deionized water: ethanol, with the volume ratio of 1:1 v/v, and then dispersed under an ultrasonication (200 W, 50 kHz) for 30 min. Afterward, the nGO solution was added to the nFe_3O_4 solution and re-ultrasonicated for an additional 30 min. This binary mixture was mixed under a stirrer for 24 h and then centrifuged at 5000 rpm (5 min) to obtain a black precipitate. Finally, the precipitate was respectively washed with deionized water and ethanol 3 times and dried at 60 °C for 12 h to obtain solid powder [24].

2.2.3 Preparation of Zif-8@nGO@nFe_3O_4

7 g of nGO@nFe_3O_4 and Zif-8 were separately added to ethanol (150 mL) and ultrasonicated for 30 min. In the following, nGO@nFe_3O_4 solution was added to Zif-8 solution and then re-ultrasonicated for 30 min. After stirring for 24 h (25 °C), black nano-precipitate was separated by centrifugation (5000 rpm, 5 min), and the obtained nanocomposite was respectively washed 3 times with deionized water, ethanol, and ether, and finally dried at 60 °C for 12 h [24].

2.3 Characterizations of the adsorbent

The morphological specifications of the fabricated samples were evaluated using a field emission scanning electron micrograph (FE-SEM, Model-MIRA2, Tescan Co., Czech Republic). The formation of the chemical bonding between materials was also assessed by Fourier-transform infrared spectroscopy (FTIR, Model-Nicolet 300, Thermo, USA), over the wavenumber range of $400-4000\ cm^{-1}$. The analysis of the crystalline structures was carried out by X-ray diffraction (XRD, PW1730-PHILIPS diffractometer) with Cu-Kα radiation ($\lambda = 1.56056\ \AA$, 2θ range: $5^\circ - 50^\circ$) at 40 keV. In the following, the composition of elements for each sample was studied by energy dispersive X-ray spectroscopy (EDS, Model-SAMX, France). The magnetic properties of samples were also assessed via the vibrating sample magnetometer analysis (VSM) (The VSM (Model-MDK, Magnatis Danesh Kavir Yazd Co., Iran) at 25 °C. Moreover, the thermal behavior of samples was studied by thermogravimetric analysis (TGA(device (TGA/DSC, Model-Q600, TA Co., USA), under an argon atmosphere (zero air), in the temperature range of $25-800$ °C at a heating rate of 15 °C/min.

2.4 Adsorption study

The dye sorption experiments by using the designed adsorbent (Zif-8@nGO@nFe_3O_4) were carried out in a discontinuous system and under a magnetic stirrer (200 rpm). Determined amount of adsorbent was stirred with the used solutions (50 mL), and the pH(s) were adjusted with HCl (0.1 N) and NaOH (0.1 N). At the end of each test, the solution and adsorbent were separated by centrifuging (5000 rpm, 10 min), and the concentration of the remained dye in the solution was determined by a spectrophotometer at 664 nm wavelength and standard curve of methylene blue. Finally, the removal efficiency (%) of the dye and the adsorption capacity of the adsorbent were respectively calculated in Eqs. (1) and (2).

$$R\% = \frac{C_0 - C_e}{C_0} \times 100 \quad (1)$$

$$q_e = \frac{v(C_0 - C_e)}{m} \quad (2)$$

where C_0 (mg/L) and C_e (mg/L), as well as v (L), and m (g) are the initial and final dye concentration, as well as the volume of dye-bearing solution, and amount of adsorbent, respectively.

2.5 Adsorption isotherm models

To understand the adsorption mechanism and analyze the experimental data, the isotherm models of the Langmuir, Freundlich, Temkin, and Redlich-Peterson were studied. These models have been listed in Table 1. Accordingly, the Langmuir model assumes that adsorbent has homogeneous surfaces and the adsorption process occurs as a monolayer. In contrast, the Freundlich isotherm assumption is that the adsorbent has a heterogeneous surface and the adsorption process is multilayer. The Temkin model assumption is also that the decreased adsorption energy occurs with coverage of the adsorbent surface. Moreover, the Redlich–Peterson model, as an empirical model and 3 parameters, derives from the combination of Langmuir and Freundlich models and can modify inexactitudes.

3. Results and discussion

3.1 Analysis of adsorbent characterizations

The morphological properties and microstructure of the designed nanocomposites were studied using FESEM. As observed in figure 1, ZIF-8 crystals possess the rhombic/cubic-polyhedral shape connected in a bead-like shape or observed individually (mean size: 133.60 nm ± 30.51) [25, 26]. Likewise, the nGO/nFe_3O_4 image indicated the morphology of nGO layers with a wrinkled characteristic with the deposition of nFe_3O_4 on its surface (owing to interactions of magnetic forces) which possessed a spherical structure with an average diameter of 34.77 nm ± 8.54. For the ZiF-8@nGO@nFe_3O_4 adsorbent, a superposition of the layered structure of nGO@nFe_3O_4 was observed which ZIF-8 was dispersed uniformly on or between the layers. Such a porous structure can promote the adsorbent active sites and improve the adsorption process.

The FT-IR spectra of samples also indicated that the ZIF-8/nGO@nFe_3O_4 adsorbent possesses a similar spectral profile to nGO@nFe_3O_4 and ZIF-8, especially in the range of $3400-3600\ cm^{-1}$ (C-O-H group) and $1350-1600\ cm^{-1}$ (imidazole ring) (figure 2) [27]. Based on the results, the absorption peaks in the range of $3000-3200\ cm^{-1}$ (3123.12 cm^{-1} and 3009.81 cm^{-1}) and at 2916.57 cm^{-1} on the ZIF-8 spectrum are related to C-H stretching vibrations in methyl group and aliphatic chain respectively in imidazole ring and 2-methylimidazole. The peaks at 1421.48 cm^{-1} and 1308.65 cm^{-1}, as well as at 759.23 cm^{-1}, 692.97 cm^{-1}, 649.57 cm^{-1}, and 619.72 cm^{-1} are also assigned to in-plane and out-of-plane bending in the imidazole ring, respectively. Moreover, observed peaks at 1576.57 cm^{-1}, 1177.05 cm^{-1}, and 995.50 cm^{-1} correspond to C=O/C=N groups and single bonds of carbon and nitrogen [28]. The peak of 420.44 cm^{-1} also belongs to the peak of the Zn-N bond between the ion Zn^{2+} and the imidazole ligand.

Table 1. Adsorption isotherm models.

Models	Linear equation	Parameters of the isotherm model
Langmuir	$\frac{C_e}{q_e} = \frac{1}{q_m K_L} + \frac{C_e}{q_m}$	q_e: Equilibrium amount of adsorbed per unit mass of adsorbent (mg/g) q_m = Maximum dye adsorption capacity (mg/g) K_L = Langmuir constant (L/mg)
Freundlich	$\log(q_e) = \log(K_F) + \frac{1}{n}\log(C_e)$	K_F = Empirical Freundlich constant (L/mg) n = Freundlich's exponent that illustrates the adsorption severity
Temkin	$q_e = B\ln(K_T) + B\ln(C_e)$	K_T = Temkin isotherm equilibrium binding constant (L/mg) B: Constant related to the heat of sorption (J/mol)
Redlich–Peterson	$\frac{C_e}{q_e} = \frac{1}{K_{RP}} + \frac{a_{RP}}{K_{RP}} C_e^{\beta}$	K_{RP} = Redlich–Peterson constant (L/g) a_{RP} = Redlich–Peterson constant (L/mg) β = Redlich–Peterson exponent

C_0 (ppm) = initial metal concentration (ppm)
C_e = Equilibrium dye concentration (ppm)

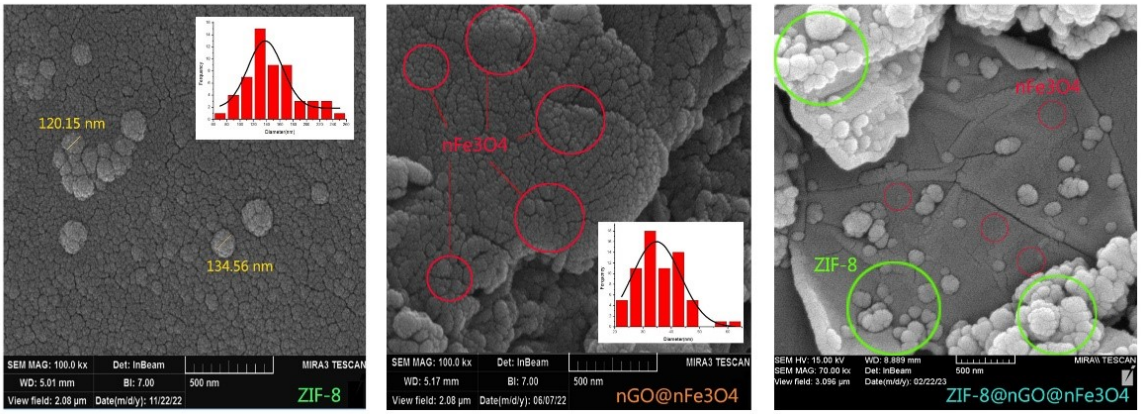

Figure 1. SEM images for the studied samples.

Shifting the position and changing the intensity of these peaks in the ZIF-8/nGO@nFe_3O_4 spectrum indicates the effective bonding of ZIF-8 with nGO@nFe_3O_4 nanocomposite. Accordingly, analysis of nGO@nFe_3O_4, nGO, and nFe_3O_4 spectra demonstrated when nGO and nFe_3O_4 are combined, the intensity of the strong peak at 589.91 cm^{-1}, in nFe_3O_4 spectrum which is related to Fe-O vibration, has significantly changed, indicating the successful synthesis of the nGO@nFe_3O_4 nanocomposite. However, when the mentioned nanocomposite decorates with ZIF-8 (i.e. ZIF-8@nGO@nFe_3O_4 spectrum), the position of peaks change, especially in the range of $600-780$ cm^{-1}, related to imidazole ring, and peak assigned to Zn-N bond which can confirm good synthesis of this adsorbent.

The XRD patterns of ZIF-8, nGO, nFe_3O_4, nGO@nFe_3O_4, and Zif-8@nGO@nFe_3O_4 are illustrated in figure 3. As observed in this figure, all XRD diagrams are at around 2θ of 5° to 50°. Based on the results, the main peaks of the ZIF-8 are obtained at 2θ among 7.31°, 10.35°, 12.65°, 14.45°, 16.50°, 17.95°, 22.08°, 24.55°, and 26.75° due to the reflection of (011), (002), (112), (022), (013), (222), (114), (233), and (134), which show good agreement with the peaks of ZIF-8 identified in other reports [28, 29], and can serve as an indication of the high purity and good crystallinity of this material. For the nGO spectrum, the sharp diffraction peak at 2θ of 11.95° corresponding to the (001) plane confirmed this material [28]. Moreover, the analysis of the nFe_3O_4 XRD diagram indicated three main sharp peaks at around 2θ at 30.33°, 35.85°, and 43.48° corresponding to crystal planes of (220), (311), and (400) respectively, which can confirm the crystalline cubic spinel structure of nFe_3O_4 [30]. The XRD pattern of nGO@nFe_3O_4 also demonstrated that the peaks of nGO and nFe_3O_4 appeared with slight shifts, at 2θ of 11.65° (for nGO) and 30.19°, 35.55°, and 43.23° (for nFe_3O_4), after decorating nGO with nFe_3O_4. It confirms the face-centered cubic lattice crystal structure and proper synthesis of this nanocomposite [31]. Regarding the ZIF-8@nGO@nFe_3O_4 nanocomposite adsorbent, the same main peaks were observed with a slight shift at 2θ, which proves the formation of this magnetic nanocomposite. Accordingly, the distinct peaks observed at 2θ among 7.39°, 10.45°, 12.78°, 14.60°, 16.53°, 18.08°, 22.09°, 24.59°, and 26.69° for ZIF-8 observed due to its crystalline nature. Furthermore, there is a prominent peak at 2θ of 11.35°, for

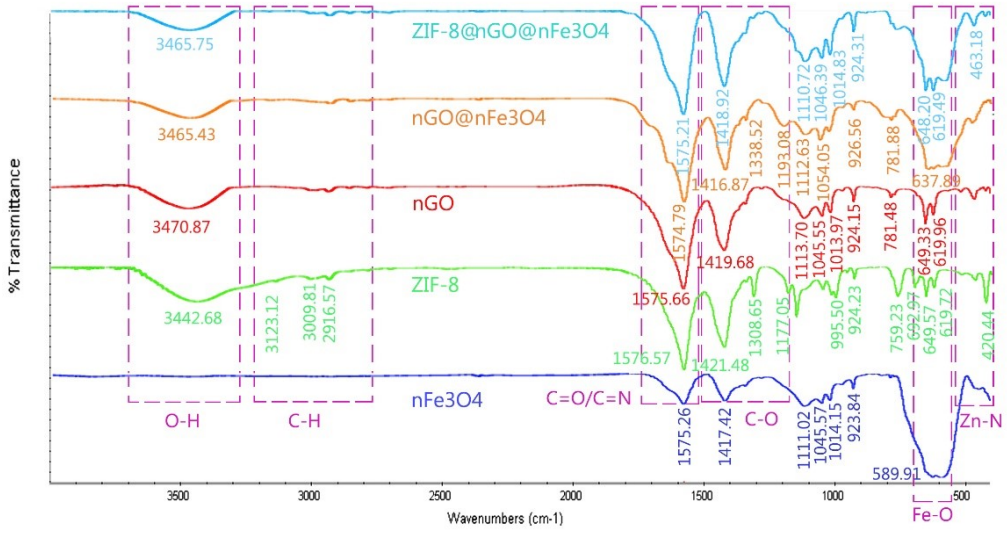

Figure 2. FTIR spectrum for the studied samples.

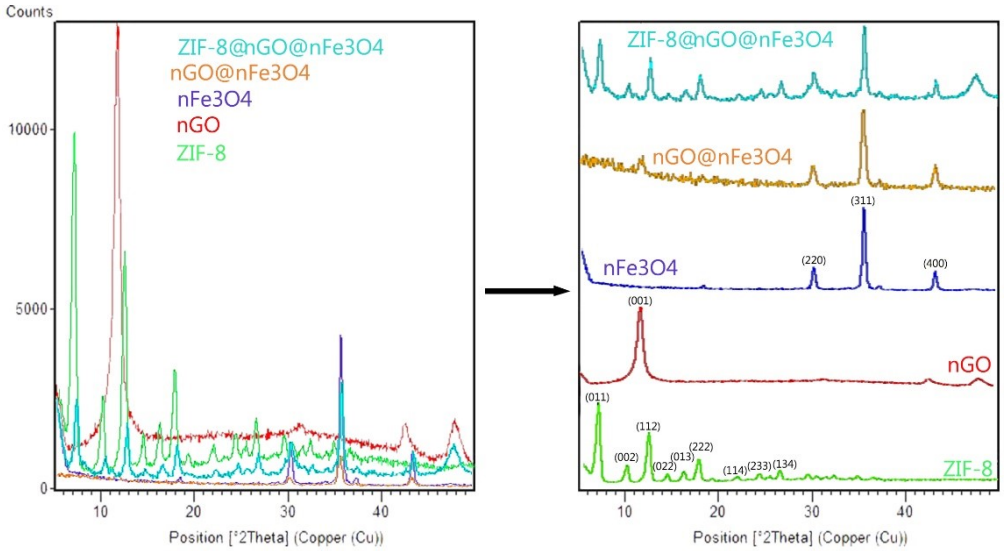

Figure 3. XRD patterns for the studied samples.

nGO, which is due to the interlayer spacing increased by the introduction of oxygen-containing groups. The peaks at around 2θ of 30.55°, 35.95°, and 43.45°, also indicated that the crystalline structure of Fe_3O_4 remained stable after decorating and coating with nGO and ZIF-8.

In the following, to further assess and determine elements in the nanocomposite structure decorated with ZIF-8, EDS analysis was carried out by energy dispersive X-ray spectroscopy. As illustrated in figure 4 (a), ZIF-8@nGO@nFe_3O_4 EDS spectrum confirmed the existence of C, N, O, Zn, and Fe elements with content (or weight percent) of 38.03 wt.%, 20.04 wt.%, 25.57 wt.%, 4.18 wt.%, and 12.18 wt.%, respectively. While this spectrum for synthesized ZIF-8 only included C, N, O, and Zn elements, respectively with weight percent of 39.00 wt.%, 48.98 wt.%, 7.05 wt.%, and 4.64 wt.%. Hence, the synthesis of ZIF-8@nGO@nFe_3O_4 magnetic nanocomposite is confirmed by observing the Iron element. Moreover,

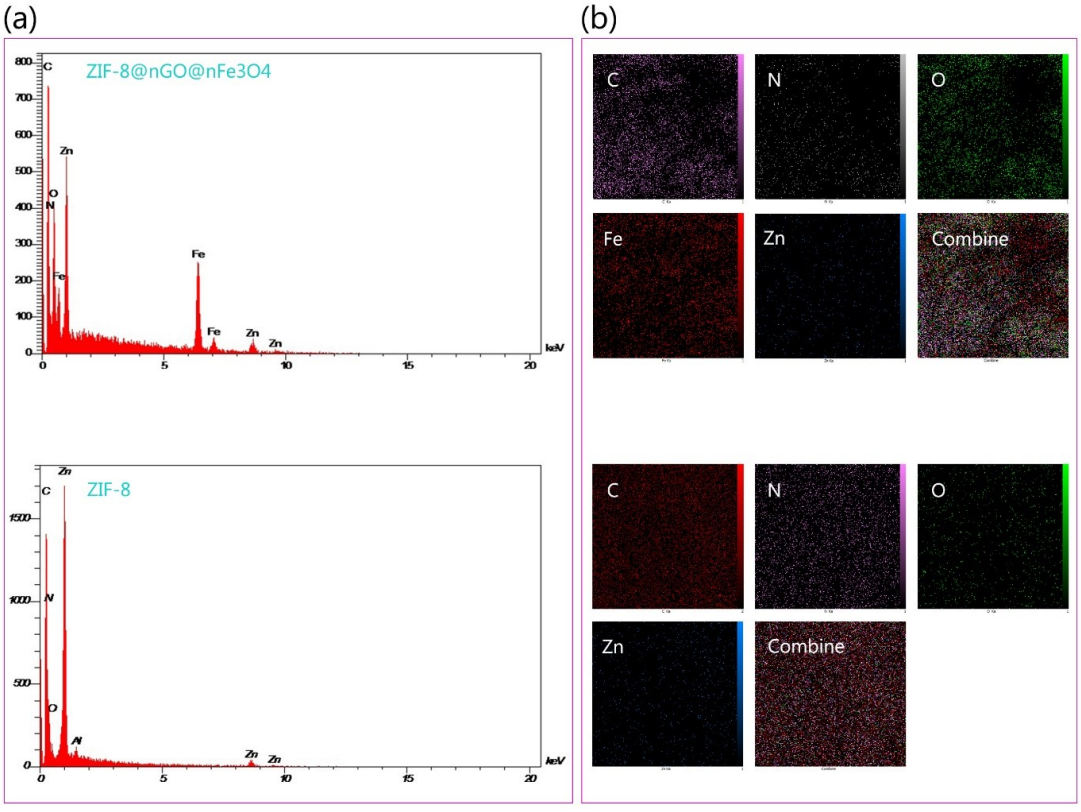

Figure 4. EDS spectra for ZIF-8@nGO@nFe_3O_4 nanocomposite adsorbent and ZIF-8 (analysis of elements (a) and elemental mapping (b)).

analysis of elemental mapping for ZIF-8@nGO@nFe_3O_4 magnetic nanocomposite (figure 4 (b)) demonstrated that Iron element is distributed across the entire surface of the nanocomposite, and the distribution of C and O also are owing to the nGO presence. Moreover, the relatively uniform distribution of Zn and N elements demonstrates the suitable growth of ZIF-8 on the surface of nGO@nFe_3O_4.

Afterward, the VSM analysis was performed to evaluate the magnetic properties of nFe_3O_4, nGO@nFe_3O_4, and ZIF-8@nGO@nFe_3O_4 nanocomposite. Based on the results, the saturation magnetization values were 66 emu/g, 28 emu/g, and 23 emu/g for nFe_3O_4, nGO@nFe_3O_4, and ZIF-8@nGO@nFe_3O_4, respectively (figure 5). Accordingly, the highest saturation magnetization value is attributed to the nFe_3O_4, and the formation of the nGO@nFe_3O_4 nanocomposite led to a reduction in this value. In the following, although decoration of the mentioned nanocomposite with ZIF-8 resulted in a further decrease in saturation magnetization due to the diamagnetic contribution of ZIF-8 surrounding nFe_3O_4, the ZIF-8@nGO@nFe_3O_4 composite adsorbent still possessed the suitable magnetic ability and easily separated by a magnet. It can confirm a good synthesis of the mentioned adsorbent.

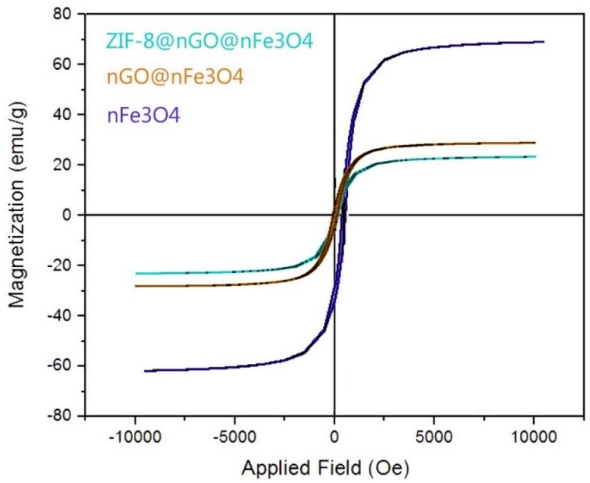

Figure 5. VSM magnetization curves for ZIF-8@nGO@nFe_3O_4, nGO@nFe_3O_4, and nFe_3O_4.

Subsequently, the thermal stability of samples was also studied by TGA analyses ($25-800°C$). Figure 6 indicates the thermal behavior of nFe_3O_4, nGO/nFe_3O_4, and ZIF-8/nGO/nFe_3O_4. As seen in this figure, for all samples, the initial segment of the TGA curve (from 25 °C to around $98-110$ °C) is related to the weight loss due to loss of water or other solvents. Afterward, the loss of weight continued due to the decomposition of bonded chains. Accordingly, the nFe_3O_4 thermal curve, except for the first stage, possessed 2 mass change stages [first a slight increase (from 98.81 °C to 391.07 °C) owing to the transformation of nFe_3O_4 to nFe_3O_4, and then a decrease (from 589.77 °C to 623.78 °C) due to the decomposition of impurities] [32]. Likewise, the nGO indicated the weight loss across the three stages (at 110.44 °C, 332.51 °C, and 472.87 °C), assigned to the decomposition of O_2 groups and the carbon lattice [33, 34]. The results also illustrated when nFe_3O_4

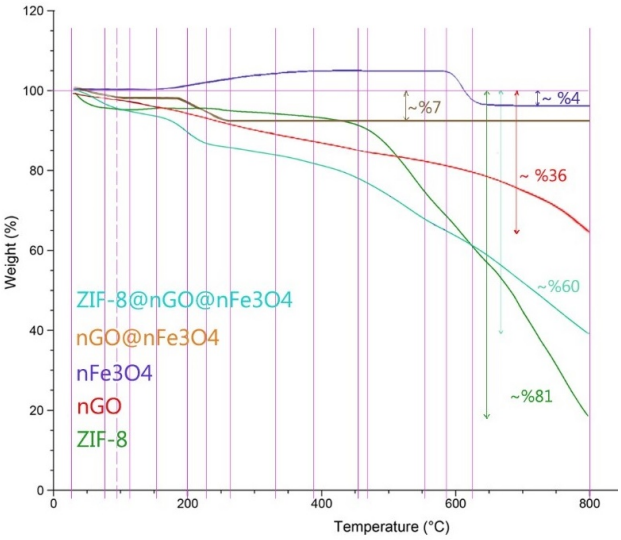

Figure 6. TGA analysis of studied samples.

and nGO are combined, no mass increase is observed for the nanocomposite of nGO@nFe_3O_4. Instead, there was a significant mass reduction in the nGO@nFe_3O_4 thermal curve compared to nFe_3O_4 (75%) which is attributed to pyrolysis of functional groups such as -OH, -C-C-O-, and C=O, as well as the decomposition of carbon skeleton. This nanocomposite indicated a thermal profile of three stages in the ranges of $100-200.12$ °C, $200.12-263.76$ °C, and $263.76-800$ °C.

For ZIF-8@nGO@nFe_3O_4, a $\sim 3\%$ weight loss was also observed up to 75.21 °C, due to the removal of surface-water molecules. In the following, 2 weight loss stages of about 6% and $\sim 14\%$ up to 154.15 °C and 226.87 °C were observed, and then this decreasing trend continued for 3 more stages (at 452.58 °C, 553.10 °C, 800 °C). These stages are mainly assigned to the decomposition of nGO and ZIF-8 the decomposition of 2-methylimidazolate and structural collapse. Based on the results, the gradual reduction in the thermal profile and lower pyrolysis temperature of ZIF-8@nGO@nFe_3O_4 compared to nFe_3O_4 and nGO can be attributed to the lower thermal stability of ZIF-8. The significant weight reduction of ZIF-8 compared to the mentioned nanocomposite adsorbent confirms this case and can prove the successful decoration of nanocomposite with ZIF-8.

3.2 Adsorption isotherm study

Adsorption isotherms are used to predict removal efficacy and assess the adsorption mechanisms. In this regard, models of Langmuir, Freundlich, Temkin, and Redlich-Peterson are widely employed for describing the equilibrium adsorption process [35, 36]. Experiments were done under optimum pH, dye concentration, adsorbent dosage, temperature, and contact time of 8, 12 ppm, 15 mg, 45 °C, and 90 min, respectively (Data was not shown). Here, the experimental data to describe the adsorption process of methylene blue on the ZIF-8@nGO@nFe_3O_4 adsorbent were assessed by these models and the parameters related to fitting each model have been demonstrated in Table 2 and figure 7.

Table 2. The parameters of isotherm models for nanocomposite adsorbent.

Isotherm	Parameters	Values
Langmuir	q_{max} (mg/g)	68.03
	K_L (L/mg)	4.454
	R_L $[R_L = \frac{1}{1+K_L C_0}]$	0.018
	R^2	0.9929
Freundlich	K_F (L/mg)	47.45
	N	4.688
	$1/n$	0.213
	R^2	0.9383
Temkin	K_T (L/mg)	584.06
	b_t $[B = \frac{RT}{b_T}]$	7.49
	B (kJ/mol)	0.331
	R^2	0.9781
Redlich–Peterson	q_{RP} (mg/g)	104.8
	K_{RP} (L/g)	4.051
	B	0.9471
	R^2	0.9955

The higher value of R^2 (0.9929) indicates a fit of the Langmuir isotherm to adsorb dye on the nanocomposite adsorbent. In this matter, the R_L value also represents that the adsorption process by these adsorbents is favorable ($0 < R_L < 1$) [37, 38]. In the following, the results indicated although the Freundlich isotherm possesses a high value of R^2 (0.9383), the Langmuir isotherm can be a better model for describing the adsorption process. This high fit indicates that the adsorbent possesses a homogeneous surface and the adsorption process is monolayer. However, given that $1/n$

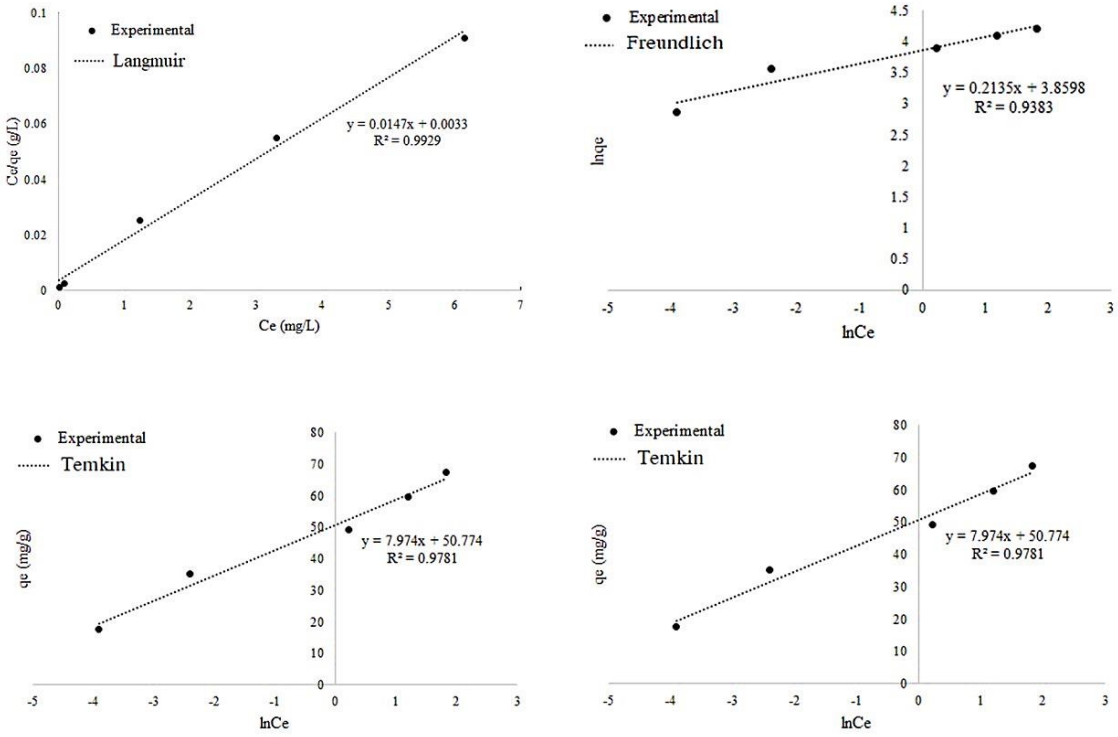

Figure 7. The equilibrium isotherm trends for dye onto ZIF-8@nGO@nFe_3O_4.

value in the Freundlich isotherm is less than 1 (Tabel 2), it can conclude that the adsorbent surface has some heterogeneities characteristics (as indicated by the relative fit of the Freundlich model), which may be due to adsorption sites with different energies or multilayer adsorption (in some area) [39]. Notably, $n > 1$ also exhibits that the adsorption process on adsorbent is controlled by physical process. The value B obtained from the Temkin model confirms this case. Indeed, if $B < 8$ kJ/mol, it indicates that the adsorption energy is relatively low, which is typically associated with physisorption [40]. In physical adsorption, interactions are mainly due to van der Waals forces, hydrogen bonds, or electrostatic interactions, which are generally non-specific [41]. This type of adsorption occurs more broadly and is less selective compared to chemical adsorption. Moreover, given that the β value in the Redlich-Peterson isotherm is close to 1 (0.9471), the results obtained from this model indicate that the Redlich-Peterson isotherm approaches the Langmuir model. This means that the adsorption is relatively monolayer and occurs on uniform adsorption sites on the surface. Likewise, *a* high β value (0.9471) suggests that the adsorbent surface is relatively homogeneous, meaning that adsorption sites with similar energy are present on the surface. It can also be inferred that the adsorption process has minimal complexity and there are relatively few interactions between the adsorbed molecules. This implies that the adsorption behavior is closer to simpler models, such as the Langmuir isotherm.

4. Conclusion

This study applied ZIF-8@nGO@nFe_3O_4 as a nanocomposite adsorbent to remove methylene blue from aqueous solutions. While, a decrease in saturation magnetization of ZIF-8@nGO@nFe_3O_4 occurred due to the diamagnetic contribution of ZIF-8 surrounding nFe_3O_4, the appropriate magnetic ability was achieved. The Langmuir isotherm excellently described the data ($R^2 = 0.9929$). Based on the results, the adsorbent possessed a homogeneous surface, and the adsorption process occurred as a monolayer. Hence, this designed adsorbent possesses substantial potential for dye removal from wastewater and can help environmental preservation.

Authors Contribution
Authors have contributed equally in preparing and writing the manuscript.

Availability of data and materials
The datasets generated (or analyzed) during the current study are available from the corresponding author on reasonable request.

Conflict of interests
The authors declare that they have no known competing financial interests or personal relationships that could have appeared to influence the work reported in this paper.

References

[1] A. Zamani, S. Asghari, and M. Tajbakhsh. "Synthesis of TiO_2/CD and TiO_2/Ag/CD Nanocomposites and Investigation of Their Visible Light Photocatalytic Activities in the Degradation of Methylene Blue.". *Chem Mehod*, **8**:177–199, 2024.
DOI: https://doi.org/10.48309/chemm.2024.432168.1753.

[2] G. Yuvaraja, C. Prasad, Y. Vijaya, and M. V. Subbaiah. "Application of ZnO nanorods as an adsorbent material for the removal of As(III) from aqueous solution: kinetics, isotherms and thermodynamic studies.". *Inter J Ind Chem*, **9**:17–25, 2018.
DOI: https://doi.org/10.1007/s40090-018-0136-5.

[3] S. Vatandoostarani, T. B. Lotfabad, A. Heidarinasab, and S. Yaghmaei. "Degradation of azo dye methyl red by Saccharomyces cerevisiae ATCC 9763.". *Int Biodeterior Biodegradation*, **125**:62–72, 2017.
DOI: https://doi.org/10.1016/j.ibiod.2017.08.009.

[4] M. Liu, Q. Chen, K. Lu, W. Huang, Z. Lü, C. Zhou, S. Yu, and C. Gao. "High efficient removal of dyes from aqueous solution through nanofiltration using diethanolamine-modified polyamide thin-film composite membrane.". *Sep Purif Technol*, **173**:135–143, 2017.
DOI: https://doi.org/10.1016/j.seppur.2016.09.023.

[5] C. S. D. Rodrigues, S. A. C. Carabineiro, F. J. Maldonado-Hódar, and L. M. Madeira. "Wet peroxide oxidation of dye-containing wastewaters using nanosized Au supported on Al_2O_3.". *Catal Today*, **280**:165–75, 2017.
DOI: https://doi.org/10.1016/j.cattod.2016.06.031.

[6] M. Auta and B. H. Hameed. "Optimized waste tea activated carbon for adsorption of Methylene Blue and Acid Blue 29 dyes using response surface methodology.". *Chem Eng J*, **175**:233–43, 2011.
DOI: https://doi.org/10.1016/j.cej.2011.09.100.

[7] G. Jethave and U. Fegade. "Design and synthesis of Zn0.3Fe0.45O3 nanoparticle for efficient removal of Congo red dye and its kinetic and isotherm investigation.". *Inter J Ind Chem*, **9**:85–97, 2018.
DOI: https://doi.org/10.1007/s40090-018-0140-9.

[8] Khiam G. Kh., R. R. Karri, N. M. Mubarak, M. Khalid, R. Walvekar, E. Ch. Abdullah, and M. E. Rahman. "Modelling and optimization for methylene blue adsorption using graphene oxide/chitosan composites via artificial neural network-particle swarm optimization.". *Mater Today Chem*, 2022.
DOI: https://doi.org/10.1016/j.mtchem.2022.100946.

[9] F. Khorasani, M. Khavarpour, S. M. Baghbanian, and S. M. Vahdat. "Zeolitic imidazolate framework/graphene oxide hybrid nanosheets functionalized chitosan/poly (2-acrylamido-2-methyl-1-propane sulfonic acid-co-sodium acrylate) for Cu (II) adsorption.". *Inter J Ind Chem*, **15**:1–12, 2024.
DOI: https://doi.org/10.57647/j.ijic.2024.1503.19.

[10] P. Ebrahimzadeh, B. Maleki, M. Ghani, and S. Peiman. "High-performance Fe_3O_4@SiO_2@Mel@DABCO catalyst for synthesis of chromene derivatives and solid phase microextraction of fipronil and prometryn in food samples followed by HPLC-UV determination.". *Chem. Method*, **8**:833–855, 2024.
DOI: https://doi.org/10.48309/chemm.2024.480851.1832.

[11] R. Heydari and M. Khavarpour. "Adsorption of malachite green from aqueous solution by nanozeolite clinoptilolite: Equilibrium, kinetic and thermodynamic studies..". *Int J Eng Trans A Basics*, **31**:1–11, 2018.

[12] Sundaram S Kumar Mallick T. Velusamy S, Roy A. "A review on heavy metal ions and containing dyes removal through graphene oxide-based adsorption strategies for textile wastewater treatment.". *Chem Rec*, **21**:1570–610, 2021.
DOI: https://doi.org/10.1002/tcr.202000153.

[13] S. M. Elgengehi, S. El-Taher, M. A. A. Ibrahim, J. K. Desmarais, and K. E. El-Kelany. "Graphene and graphene oxide as adsorbents for cadmium and lead heavy metals: A theoretical investigation.". *Appl Surf Sci*, **507**:145038, 2020.
DOI: https://doi.org/10.1016/j.apsusc.2019.145038.

[14] K. Thakur and B. Kandasubramanian. "Graphene and graphene oxide-based composites for removal of organic pollutants: A review.". *J Chem Eng Data*, **64**:833–67, 2019.
DOI: https://doi.org/10.1021/acs.jced.8b01057.

[15] N. Wu, C. Liu, D. Xu, J. Liu, W. Liu, Q. Shao, et al. "Enhanced electromagnetic wave absorption of three-dimensional porous Fe_3O_4/C composite flowers.". *ACS Sustain Chem Eng*, **6**:12471–80, 2018.
DOI: https://doi.org/10.1021/acssuschemeng.8b03097.

[16] S. B. Zadvarzi, M. Khavarpour, S. M. Vahdat, S. M. Baghbanian, Rad, and A. S. "Synthesis of Fe_3O_4@chitosan@ZIF-8 towards removal of malachite green from aqueous solution: Theoretical and experimental studies.". *Int J Biol Macromol*, **168**:428–41, 2021.
DOI: https://doi.org/10.1016/j.ijbiomac.2020.12.067.

[17] S. Peiman, B. Maleki, and M. Ghani. "Fe_3O_4@SiO_2@Mel-Rh-Cu: A High-Performance, Green Catalyst for Efficient Xanthene Synthesis and Its Application for Magnetic Solid Phase Extraction of Diazinon Followed by Its determination through HPLC-UV.". *Int Chem Method.*, **8**:257–278, 2024.
DOI: https://doi.org/10.48309/chemm.2024.442693.1767.

[18] H. Mittal and Mishra S. B. "Gum ghatti and Fe_3O_4 magnetic nanoparticles based nanocomposites for the effective adsorption of rhodamine B.". *Carbohydr Polym*, **101**:1255–64, 2014.
DOI: https://doi.org/10.1016/j.carbpol.2013.09.045.

[19] J. Troyano, A. Carné-Sánchez, C. Avci, I. Imaz, and D. Maspoch. "Colloidal metal–organic framework particles: the pioneering case of ZIF-8.". *Chem Soc Rev*, **48**:5534–46, 2019.
DOI: https://doi.org/10.1039/C9CS00472F.

[20] K. Li, N. Miwornunyuie, L. Chen, H. Jingyu, P. S. Amaniampong, D. A. Koomson, D. Ewusi-Mensah, W. Xue, G. Li, and H. Lu. "Sustainable application of ZIF-8 for heavy-metal removal in aqueous solutions.". *Sustain*, **13**:984, 2021.
DOI: https://doi.org/10.3390/su13020984.

[21] X. Chang, P. Hu, H. Liu, Z. Lv, J. Yang, J. Wang, Zh. Li, L. Qian, and W. Wu. "ZIF-8 modified graphene oxide/sodium alginate 3D elastic spheres for uranium trapping in seawater.". *Desalination*, **549**:1163–71, 2023.
DOI: https://doi.org/10.1016/j.desal.2023.116371.

[22] P. Xu, G. M. Zeng, D. L. Huang, C. L. Feng, S. Hu, M. H. Zhao, C. Lai, Zh. Wei, Ch. Huang, G. X. Xie, and Zh. F. Liu. "Use of iron oxide nanomaterials in wastewater treatment: a review.". *Sci Total Environ*, **424**:1–10, 2012.
DOI: https://doi.org/10.1016/j.scitotenv.2012.02.023.

[23] J. Cravillon, S. Münzer, S-J. Lohmeier, A. Feldhoff, K. Huber, and M. Wiebcke. "Rapid Room-Temperature Synthesis and Characterization of Nanocrystals of a Prototypical Zeolitic Imidazolate Framework.". *Chem Mater*, **21**:1410–2, 2009.
DOI: https://doi.org/10.1021/cm900166h.

[24] M. Marcos-Hernández, R. A. Arrieta, K. Ventura, J. Hernández, C. D. Powell, A. J. Atkinson, J. S. Markovski, J. Gardea-Torresdey, K. D. Hristovski, P. Westerhoff, M. S. Wong, and D. Villagran. "Superparamagnetic nanoadsorbents for the removal of trace As(III) in drinking water.". *Environ Adv*, **4**:100046, 2021.
DOI: https://doi.org/10.1016/j.envadv.2021.100046.

[25] W. Xue, Q. Zhou, F. Li, and B. S. Ondon. "Zeolitic imidazolate framework-8 (ZIF-8) as robust catalyst for oxygen reduction reaction in microbial fuel cells.". *J Power Sources*, **423**:9–17, 2019.
DOI: https://doi.org/10.1016/j.jpowsour.2019.03.017.

[26] P. Pillai, S. Dharaskar, S. Sasikumar, and M. Khalid. "Zeolitic imidazolate framework-8 nanoparticle: a promising adsorbent for effective fluoride removal from aqueous solution.". *Appl Water Sci*, **9**:150, 2019.
DOI: https://doi.org/10.1007/s13201-019-1030-9.

[27] B. Sarwar, A. U. Khan, M. Aslam, A. Bokhari, M. Mubashir, A. A. Alothman, M. Ouladsmane, S. A. Aldossari, W. S. Chai, and K. Sh. Khoo. "Comparative study of ZIF-8-materials for removal of hazardous compounds using physio-chemical remediation techniques.". *Environ Res*, **220**:1–11, 2023.
DOI: https://doi.org/10.1016/j.envres.2022.115168.

[28] F. Chu, Y. Zheng, B. Wen, L. Zhou, J. Yan, and Y. Chen. "Adsorption of toluene with water on zeolitic imidazolate framework-8/graphene oxide hybrid nanocomposites in a humid atmosphere.". *RSC Adv*, **8**:2426–32, 2018.
DOI: https://doi.org/10.1039/C7RA12931A.

[29] A. Jaafar, S. El-Husseini, C. Platas-Iglesias, and R. A. Bilbeisi. "Zeolitic imidazolate framework (AMCD-ZIF) functionalised membrane for the removal of dyes from water.". *J Environ Chem Eng*, **10**:1–10, 2022.
DOI: https://doi.org/10.1016/j.jece.2022.108019.

[30] T. Yang, C. Shen, Z. Li, H. Zhang, C. Xiao, S. Chen, et al. "Highly Ordered Self-Assembly with Large Area of Fe_3O_4 Nanoparticles and the Magnetic Properties.". *J Phys Chem B*, **109**:23233–6, 2005.
DOI: https://doi.org/10.1021/jp054291f.

[31] I. Anshori, K. A. A. Kepakisan, Nuraviana Rizalputri L., R. Rona Althof, A. E. Nugroho, R. Siburian, and M. Handayani. "Facile synthesis of graphene oxide/Fe_3O_4 nanocomposite for electrochemical sensing on determination of dopamine.". *Nanocomposites*, **8**:155–66, 2022.
DOI: https://doi.org/10.1080/20550324.2022.2090050.

[32] T. Wang, L. Zhang, C. Li, W. Yang, T. Song, C. Tang, Y. Meng, Sh. Dai, H. Wang, L. Chai, and J. Luo. "Synthesis of Core–Shell Magnetic Fe_3O_4@poly (m -Phenylenediamine) Particles for Chromium Reduction and Adsorption.". *Environ Sci Technol*, **49**:5654–62, 2015.
DOI: https://doi.org/10.1021/es5061275.

[33] S. Stankovich, D. A. Dikin, R. D. Piner, K. A. Kohlhaas, A. Kleinhammes, Y. Jia, Y. Wu, S. Nguyen, and R. Ruoff. "Synthesis of graphene-based nanosheets via chemical reduction of exfoliated graphite oxide.". *Carbon N Y*, **45**:1558–65, 2007.
DOI: https://doi.org/10.1016/j.carbon.2007.02.034.

[34] Q. Yang, R. Lu, S. Ren, C. Chen, Z. Chen, and X. Yang. "Three dimensional reduced graphene oxide/ZIF-67 aerogel: Effective removal cationic and anionic dyes from water.". *Chem Eng J*, **348**:202–11, 2018.
DOI: https://doi.org/10.1016/j.cej.2018.04.176.

[35] H. Esmaeili and R. Foroutan. "Adsorptive Behavior of Methylene Blue onto Sawdust of Sour Lemon, Date Palm, and Eucalyptus as Agricultural Wastes.". *J Dispers Sci Technol*, **40**:990–9, 2019.
DOI: https://doi.org/10.1080/01932691.2018.1489828.

[36] D. Ramutshatsha-Makhwedzha, A. Mavhungu, M. L. Moropeng, and R. Mbaya. "Activated carbon derived from waste orange and lemon peels for the adsorption of methyl orange and methylene blue dyes from wastewater.". *Heliyon*, **8**:e09930, 2022.
DOI: https://doi.org/10.1016/j.heliyon.2022.e09930.

[37] Y. Bulut and Z. Tez. "Adsorption studies on ground shells of hazelnut and almond.". *J Hazard Mater*, **149**:35–41, 2007.
DOI: https://doi.org/10.1016/j.jhazmat.2007.03.044.

[38] Y. Bulut, N. Gözübenli, and H. Aydın. "Equilibrium and kinetics studies for adsorption of direct blue 71 from aqueous solution by wheat shells.". *J Hazard Mater*, **144**:300–6, 2007.
DOI: https://doi.org/10.1016/j.jhazmat.2006.10.027.

[39] A. R. Yari, F. Kord Mostafapour, Y. Mahdavi, and A. Joghataei. "Agricultural Waste as Adsorbent for Removal of Chromium (VI) from aqueous solution.". *Arch Hyg Sci*, **5**:310–8, 2016.

[40] J. Serafin and B. Dziejarski. "Application of isotherms models and error functions in activated carbon CO_2 sorption processes.". *Microporous Mesoporous Mater*, **354**:112513, 2023.
DOI: https://doi.org/10.1016/j.micromeso.2023.112513.

[41] P. Zhang, Y-P. Chen, and J-S. Guo. "SPR for water pollutant detection and water process.". *Analysis*, **95**:145–83, 2021.
DOI: https://doi.org/10.1016/bs.coac.2021.06.001.